

# Effects of domain walls and chiral supercurrent in quantum anomalous Hall Josephson junctions

Junjie Qi,<sup>1,\*</sup> Haiwen Liu,<sup>2</sup> Jie Liu,<sup>3</sup> Hua Jiang,<sup>4</sup> Dong E. Liu,<sup>5, 1, 6, 7</sup> Chui-Zhen Chen,<sup>8, 9, †</sup> Ke He,<sup>5, 1, 6, 7</sup> and X. C. Xie<sup>10, 4, 7</sup>

<sup>1</sup>*Beijing Academy of Quantum Information Sciences, Beijing 100193, China*

<sup>2</sup>*Center for Advanced Quantum Studies, Department of Physics, Beijing Normal University, Beijing 100875, China*

<sup>3</sup>*School of Physics, Xi'an Jiaotong University, Ministry of Education Key Laboratory for Non-Equilibrium Synthesis and Modulation of Condensed Matter, Xi'an 710049, China*

<sup>4</sup>*Institute for Nanoelectronic Devices and Quantum Computing, Fudan University, Shanghai 200433, China*

<sup>5</sup>*State Key Laboratory of Low Dimensional Quantum Physics, Department of Physics, Tsinghua University, Beijing 100084, China*

<sup>6</sup>*Frontier Science Center for Quantum Information, Beijing 100084, China*

<sup>7</sup>*Hefei National Laboratory, Hefei 230088, China*

<sup>8</sup>*School of Physical Science and Technology, Soochow University, Suzhou 215006, China*

<sup>9</sup>*Institute for Advanced Study, Soochow University, Suzhou 215006, China*

<sup>10</sup>*International Center for Quantum Materials, School of Physics, Peking University, Beijing 100871, China*

The intriguing interplay between topology and superconductivity has attracted significant attention, given its potential for realizing topological superconductivity. In this study, we investigate the transport properties of the chiral Josephson effect in the quantum anomalous Hall insulators (QAHI)-based junction. We reveal a systematic crossover from edge-state to bulk-state dominant supercurrents, with a notable  $0 - \pi$  transition observed under non-zero magnetic flux through chemical potential adjustments. This transition underscores the competition between bulk and chiral edge transport. Furthermore, we identify an evolution among three distinct quantum interference patterns: from a  $2\Phi_0$ -periodic oscillation pattern, to a  $\Phi_0$ -periodic oscillation pattern, and then to an asymmetric Fraunhofer pattern ( $\Phi_0 = h/2e$  is the flux quantum,  $h$  the Planck constant, and  $e$  the electron charge). Subsequently, we examine the influence of domains on quantum interference patterns. Intriguingly, a distinctive Fraunhofer-like pattern, with periods twice those of the conventional one, emerges due to the coexistence of chiral edge states and domain wall states, even when the chemical potential is within the gap. These results not only advance the theoretical understanding but also pave the way for the experimental discovery of the chiral Josephson effect based on QAHI doped with magnetic impurities.

## I. INTRODUCTION

Quantum anomalous Hall insulators (QAHI) have emerged as distinctive topological materials in recent decades [1–4]. One of their prominent features is the presence of unidirectional chiral edge states, observable even in the absence of external magnetic fields. The QAHI states have been theoretically predicted in various materials [5–7] and experimentally confirmed in films doped with Cr in  $(\text{Bi}, \text{Sb})_2\text{Te}_3$  [8–17], V in  $(\text{Bi}, \text{Sb})_2\text{Te}_3$  [10, 18–22],  $\text{MnBi}_2\text{Te}_4$  [23–25], and recently moiré superlattice systems [26–28]. Remarkably, the proximity of a QAHI to an s-wave superconductor (SC) was predicted to potentially realize a chiral topological superconductor within these heterostructures via the superconducting proximity effect [29, 30]. Therefore, QAHI/SC heterostructures have garnered considerable attention as promising platforms for realizing topological superconductors [29, 31–42]. More interestingly, when a QAHI is sandwiched by two QAHI/SC heterostructures, a chi-

ral Josephson junction (JJ) can be formed. Investigating JJs based on QAHI provides insights into the interplay between topology and superconductivity, offering the potential for novel phenomena and applications in quantum information processing and topological quantum computing [43–47].

As illustrated in Fig. 1(a), the chiral JJ is formed by attaching two superconducting electrodes to the top of the QAHI. Typically, the supercurrent within the JJ is carried by Andreev bound states, a consequence of successive Andreev reflections (ARs) occurring at the two QAHI-SC interfaces. Each AR involves the conversion of an electron into a hole that occurs at the QAHI-SC interface [48], which is accompanied by the creation of a Cooper pair in the superconducting region. For example, an electron propagating along the top edge may experience a crossed (non-local) AR (CAR) process at the QAHI-SC interface in the absence of bulk carriers. This process would result in the electron changing into a hole at the bottom edge and the formation of an Andreev pair (see Fig. 1(b)). Thus, the critical Josephson current  $I_c$  in response to the external magnetic flux  $\Phi$  can be described theoretically by the periodicity of  $2\Phi_0$  [44, 49–54], where  $\Phi_0 = h/2e$  is the flux quantum,  $h$  the Planck constant, and  $e$  the electron charge. The period

\* qijj@baqis.ac.cn

† czchen@suda.edu.cn

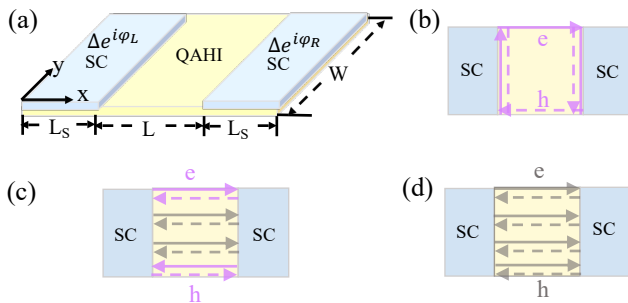


FIG. 1. (a) Schematic diagram of a QAHI-based JJ. The QAHI is partially covered by two superconducting electrodes. The central region and the superconducting region have sizes of  $W \times L$  and  $W \times L_s$ , respectively. (b) Schematic diagram of CARs in real space, where Andreev pairs are constituted by electrons and holes propagating along opposing edges. (c) Schematic diagram of LARs in real space, depicting the formation of Andreev pairs primarily from edge carriers at a single edge. Additionally, Andreev pairs are present in the inner QAHI region, as a result of the bulk carriers. This particular regime results in transport being predominantly governed by edge carriers. (d) Schematic diagram of LARs in real space, where Andreev pairs formed by bulk carriers exhibit uniform distribution within the central region. In Figs. (b)-(d), we use purple (gray) lines to represent edge (bulk) carriers, respectively.

is twice that of the conventional Aharonov-Bohm (AB) oscillations. However, there are two important questions that must be addressed in realistic JJs. First, during experimental measurements, bulk carriers may participate in the transport process in realistic JJs. Observing the evolution of the quantum interference pattern with respect to the ratio of bulk carriers to chiral edge carriers as the chemical potential  $\mu$  is altered is desirable. Second, in the magnetically doped QAHI region, domain walls (DWs) are an inevitable presence. The effects of the DWs on the quantum interference pattern are worth studying.

In this work, we systematically explore a JJ based on a QAHI with realistic magnetic domains, aiming to address the two aforementioned questions. The Josephson current  $I_s$  is calculated by the recursive Green-function method. First, we look into the evolution of the current-phase relation as a function of the chemical potential  $\mu$ . A notable  $0 - \pi$  transition is observed under a non-zero magnetic flux, when the chiral edge states penetrate into the bulk region. Then, we display the critical Josephson current  $I_c$  as a function of the magnetic flux  $\Phi$  for various chemical potentials  $\mu$ . We find three distinct quantum interference patterns: a  $2\Phi_0$ -periodic oscillation pattern, a  $\Phi_0$ -periodic oscillation pattern, and an asymmetric Fraunhofer pattern. These three interference patterns indicate different AR processes as shown in Figs. 1(b)-(d). Further, we examine the effects of DWs on the  $2\Phi_0$ -periodic oscillation pattern and asymmetric Fraunhofer pattern. We find that the asymmetric Fraun-

hofer pattern is very robust against the DWs, while the  $2\Phi_0$ -periodic oscillation pattern is susceptible to modest magnetic fluctuations. Remarkably, a Fraunhofer-like pattern, with periods twice those of the conventional one, emerges when the chiral edge state and magnetic domain wall states coexist at  $\mu = 0$ . The observed Fraunhofer-like pattern is expected to extend beyond our model and could be prevalent in materials doped with magnetic impurities, suggesting potential for further experimental verification.

The paper is organized as follows. We introduce the model employed in this work in Sec. II. Sec. III presents the key findings of our calculations and the corresponding remarks. More specifically, in Sec. III A, we study the current-phase relation as a function of chemical potential  $\mu$  and observe a  $0 - \pi$  transition when the chiral edge states at the left and right QAHI-SC interfaces overlap in space with non-zero magnetic flux  $\Phi$ . Sec. III B discusses three distinct quantum interference patterns. The effects of DWs, which are covered in Sec. III C, inevitably occur in the magnetically doped topological insulators. We find that the  $2\Phi_0$ -periodic oscillation effect is destroyed by modest magnetic fluctuations. A Fraunhofer-like pattern is observed even when  $\mu = 0$ . Sec. IV is the conclusion.

## II. MODEL

As depicted in Fig. 1(a), the QAHI-based junction comprises three parts: two superconducting electrodes and a central region with QAHI. The  $4 \times 4$  low-energy effective Hamiltonian describing magnetic topological insulator thin films in the central region is given by [55, 56]

$$H(\mathbf{k}) = \hbar v_F (k_y \sigma_x \tau_z - k_x \sigma_y \tau_z) + m(\mathbf{k}) \tau_x + M_z \sigma_z \quad (1)$$

in the basis of  $\psi_{\mathbf{k}} = [\psi_{\mathbf{k},t\uparrow}, \psi_{\mathbf{k},t\downarrow}, \psi_{\mathbf{k},b\uparrow}, \psi_{\mathbf{k},b\downarrow}]^T$  with the wave vector  $\mathbf{k}$ .  $\uparrow$  ( $\downarrow$ ) represents the spin direction, and  $t$  ( $b$ ) denotes the surface states of the top (bottom) layer. The symbols  $\sigma_{x,y,z}$  and  $\tau_{x,y,z}$  correspond to the Pauli matrices for spin and layer, respectively.  $M_z$  represents the exchange field along the  $z$  axis induced by the ferromagnetic ordering. The term  $m(\mathbf{k}) = m_0 - m_1 \mathbf{k}^2$  describes the coupling between the top and bottom surface states. The system is in the QAHI phase with the Chern number  $C = \text{sgn}(M_z)$  when  $|M_z| > |m_0|$ , while it is a normal insulator with  $C = 0$  when  $|M_z| < |m_0|$ .

In our numerical simulations, we discretize the Hamiltonian in Eq. 1 to a tight-binding model in a square lattice as [45]

$$H = \sum_{ij} \left( \psi_i^\dagger t_0 \psi_j + \psi_i^\dagger t_x \psi_{i+\hat{x}} + \psi_i^\dagger t_y \psi_{i+\hat{y}} + \text{H.c.} \right) \quad (2)$$

where  $\hat{x}$  ( $\hat{y}$ ) the unit vector along the  $x$  ( $y$ ) axis and  $i$  the

site index. The  $4 \times 4$  matrices  $t_{0,x,y}$  are given by

$$\begin{aligned} t_0 &= \left( m_0 - 4 \frac{m_1}{a^2} \right) \tau_x \sigma_0 + M_z \tau_0 \sigma_z, \\ t_x &= \left( \frac{m_1}{a^2} \tau_x \sigma_0 + \frac{i v_F}{2a} \tau_z \sigma_y \right) e^{i \phi_{i,i+\hat{x}}}, \\ t_y &= \frac{m_1}{a^2} \tau_x \sigma_0 - \frac{i v_F}{2a} \tau_z \sigma_x. \end{aligned}$$

where  $t_x$  gains a phase  $\phi_{ij} = \pi \int_i^j \mathbf{A} \cdot d\mathbf{l} / \Phi_0$  due to the magnetic field  $B$  in  $z$  direction with the vector potential  $\mathbf{A} = (-yB, 0, 0)$ , and  $\Phi_0 = h/2e$  is the flux quantum with the Planck constant  $h$  and the elementary charge  $e$ . Here  $\sigma_0$  ( $\tau_0$ ) denotes the  $2 \times 2$  identity matrix. The total magnetic flux of the central region is denoted as  $\Phi$ . The parameters are set as follows: lattice constant  $a = 1$ , Fermi velocity  $v_F = 1$ ,  $m_1 = 1$ , and  $m_0 = -0.1$ .

In proximity to an s-wave SC, a finite pair amplitude is induced in the QAHI. The Bogoliubov-de Gennes (BdG) Hamiltonian of QAHI/SC heterostructures in Nambu space is given by  $H_{\text{BdG}} = \sum_{\mathbf{k}} \Psi_{\mathbf{k}}^\dagger H_{\text{BdG}}(\mathbf{k}) \Psi_{\mathbf{k}} / 2$  with  $\Psi_{\mathbf{k}} = [(\Psi_{\mathbf{k},t\uparrow}, \Psi_{\mathbf{k},t\downarrow}, \Psi_{\mathbf{k},b\uparrow}, \Psi_{\mathbf{k},b\downarrow}), (\Psi_{-\mathbf{k},t\uparrow}^\dagger, \Psi_{-\mathbf{k},t\downarrow}^\dagger, \Psi_{-\mathbf{k},b\uparrow}^\dagger, \Psi_{-\mathbf{k},b\downarrow}^\dagger)]^T$  and

$$\begin{aligned} H_{\text{BdG}}(\mathbf{k}) &= \begin{pmatrix} H(\mathbf{k}) - \mu & \Delta \\ \Delta^\dagger & -H^*(-\mathbf{k}) + \mu \end{pmatrix}, \\ \Delta &= \begin{pmatrix} i e^{i\varphi_{L(R)}} \Delta_t \sigma_y & 0 \\ 0 & i e^{i\varphi_{L(R)}} \Delta_b \sigma_y \end{pmatrix}. \end{aligned} \quad (3)$$

Here  $\mu$  is the chemical potential,  $\varphi_L$  and  $\varphi_R$  are the superconducting phases in the left and right sides of the junction. The physical properties only depend on the superconducting phase difference  $\varphi = \varphi_L - \varphi_R$ .  $\Delta_t$  and  $\Delta_b$  denote the induced superconducting pairing potentials on the top and bottom surface states, respectively. For simplicity, we set  $\Delta_t = 0.5$  and  $\Delta_b = 0$  in the following calculations, and both the QAHI and superconducting regions have dimensions  $W \times L(L_s) = 100 \times 40$ .

### III. NUMERICAL RESULTS

#### A. Current-phase relation

To start with, we investigate the current-phase relation with varying the chemical potential  $\mu$  in the pure JJ, as shown in Figs. 2(a) and (b). The Josephson current is computed employing the recursive Green-function method as proposed in Refs. [57–59]. In Fig. 2(a), the current-phase relation of  $I_s/I_c$  exhibits a period of  $2\pi$  and displays a typical sinusoidal shape when  $\mu = 0, 0.1, 0.21$  with a magnetic flux  $\phi = 0$ . Note that it slightly deviates from the sinusoidal relation when  $\mu = 0.4, 0.7, 1$ . Notably, upon introducing  $\Phi$  to the QAHI region, a magnetic field-controlled  $0 - \pi$  transition is observed at  $\mu = 0.21$  with  $\phi = 0.0024$  in Fig. 2(b).

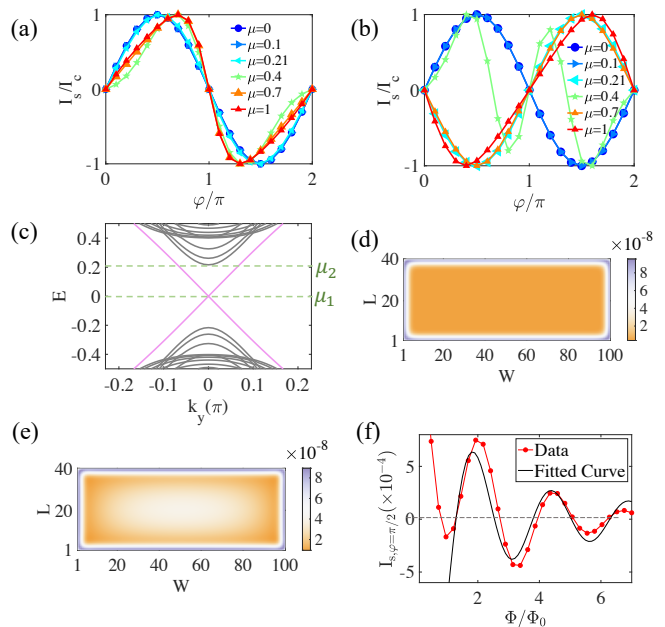


FIG. 2. The normalized supercurrent  $I_s/I_c$ , where  $I_c$  is the critical Josephson current, changes with (a) the superconducting phase difference  $\varphi$  when  $\phi = 0$ , and (b) when  $\phi = 0.0024$ , where  $\phi$  denotes the magnetic flux on each lattice. Different colored curves correspond to different values of the chemical potential  $\mu$ . (c) The QAHI energy spectrum with a length of  $L = 40$  is calculated by using a lattice model described by Eq. 2.  $\mu_1 = 0$  and  $\mu_2 = 0.21$  are the chemical potentials, indicated by the green dashed lines. Density of states of (d)  $\mu_1 = 0$  and (e)  $\mu_2 = 0.21$  in the QAHI region. (f) The supercurrent  $I_s$  with the superconducting phase difference  $\varphi = \pi/2$  as a function of the total magnetic flux of the central region  $\Phi$  for the chemical potential  $\mu = 0.21$ . In all cases, we take  $M_z = 0.3$  and the temperature  $T = \Delta/200$ .

To grasp the origin of this transition, we examine the density of states in the QAHI region corresponding to the Fermi energies  $\mu_1 = 0$  and  $\mu_2 = 0.21$ , depicted in Figs. 2(d) and (e). When  $\mu_1 = 0$ , the states localize at the left and right QAHI-SC interfaces without any presence of bulk carriers in the QAHI region, resulting solely in CARs. Conversely, by shifting  $\mu$  to 0.21, the density of states distinctly shows that the states at both the left and right QAHI-SC interfaces broaden and spatially overlap. This broadening allows the supercurrent to flow across the QAHI bulk region, resulting in the occurrence of LARs occur along with the CARs. In this case, this supercurrent under the influence of magnetic flux exhibits behavior akin to the Fraunhofer pattern, expressed as  $I_s \propto \frac{\sin(\pi\Phi/\Phi_0)}{\pi\Phi/\Phi_0} \sin(\varphi)$ . Consequently, at certain magnetic flux values, a  $0 - \pi$  transition may occur. To support this statement, we plot the supercurrent  $I_s$  as a function of  $\Phi$  for  $\varphi = \pi/2$ , fitting the data points to the ideal Fraunhofer pattern, illustrated in Fig. 2(f). The observed slight deviation from the ideal Fraunhofer pattern fit may stem from the inhomogeneous carrier density within the QAHI

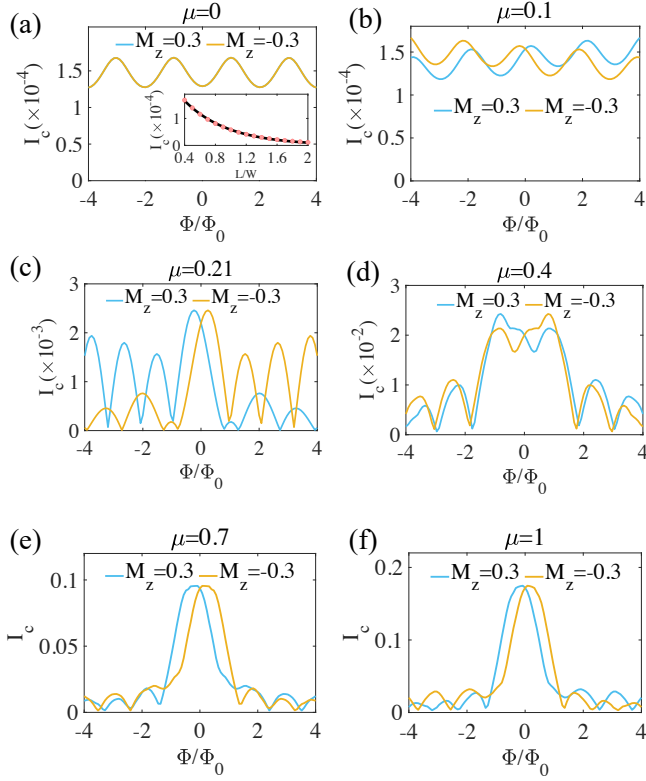


FIG. 3. Quantum interference patterns in different regimes. The critical Josephson current  $I_c$  versus the magnetic flux  $\Phi$  in the unit of  $\Phi_0$ . (a) CARs happen when only chiral edge states are included with  $\mu = 0$ .  $I_c$  exhibits the unconventional AB oscillation characterized by a periodicity of  $2\Phi_0$ . The inset showcases the dependence of  $I_c$  on the aspect ratio  $L/W$  (depicted as red circles), and a fitting curve is provided as a solid black line. We take  $M_z = 0.3$ . (b)-(e) The behavior of  $I_c$  deviates from the  $2\Phi_0$ -periodic oscillation as  $\mu$  takes on values of 0.1, 0.21, 0.4, and 0.7, respectively. (c) The wavefunctions at the left and right edges exhibit overlapping behavior, making the occurrence of LARs at a single edge.  $I_c$  is notably marked by a  $\Phi_0$  periodicity. It is noteworthy that when  $\mu > 0.21$ , bulk carriers actively engage in the transport process. (d) The emergence of central and side lobes is a consequence of the interference pattern transitioning towards a regime dominated by bulk carriers. (f)  $I_c$  displays the typical asymmetric Fraunhofer pattern with  $\mu = 1$ . In this regime, the bulk carriers uniformly flow through the whole QAHI region. In all cases, the blue (orange) solid lines represent  $I_c$  curves corresponding to  $M_z = \pm 0.3$ .

region. Therefore, we conclude that the  $0 - \pi$  transition underscores the crossover from the chiral-edge to bulk dominant transport.

### B. Three distinct quantum interference patterns

Next, we examine the quantum interference patterns within the QAHI-based junction. At a chemical potential of  $\mu = 0$ , as depicted in Fig. 3(a), the QAHI region exclu-

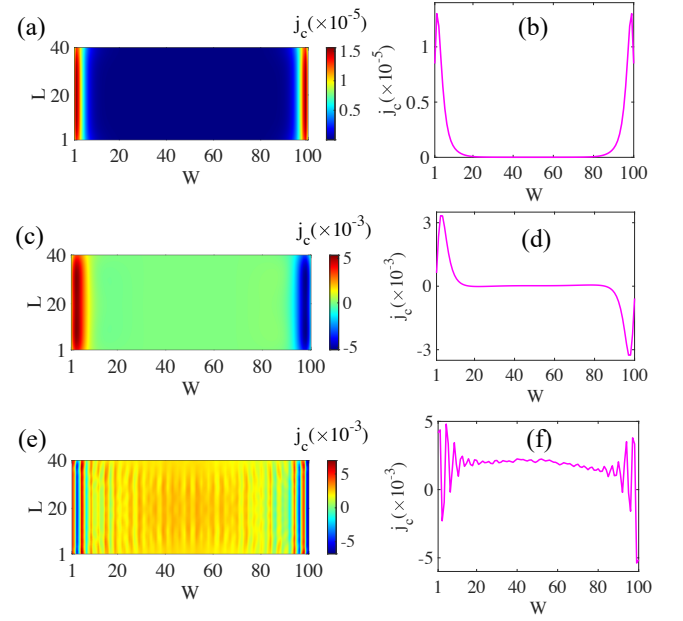


FIG. 4. The spatial distribution of local critical current in the QAHI region [(a), (c), and (e)] and at the QAHI-SC interface [(b), (d), and (f)] is examined under varying chemical potentials:  $\mu = 0$  [(a), (b)], 0.21 [(c), (d)], and 1 [(e), (f)]. In all cases,  $M_z = 0.3$ ,  $\Phi = 0$ , and the temperature  $T = \Delta/200$ .

sively accommodates chiral edge carriers. At the interface between the QAHI and the SC, an electron from one chiral edge mode can tunnel into a hole on the opposite edge through the CAR process. Similarly, the holes are then reflected as electrons along the other QAHI-SC interface. This entire process forms a loop, completing the transfer of the supercurrent, and leading to an intriguing AB oscillation pattern. This interference pattern, a hallmark of chiral edge states, exhibits two distinctive features: (1) Unlike the conventional  $\Phi_0$  periodicity, the critical Josephson current  $I_c$  has a periodicity of  $2\Phi_0$ . (2) The minima of  $I_c$  are non-zero. These findings align with prior research studies [44, 49–54]. We note that the exponential decay of the peak value of  $I_c$  with the aspect ratio  $L/W$  is suitably described by the equation  $I_c \propto \exp(-\alpha L/W)$  (see the inset of Fig. 3(a)), where  $\alpha$  is a fitting constant. Furthermore, by shifting the chemical potential to  $\mu = 0.1$ , an observed phase shift arises from the finite chemical potential. This occurrence is tied to the sustenance of the Josephson current by Andreev bound states forming a closed loop. Consequently, the product of the Fermi wavelength and the circumference,  $k_F * L_d$ , introduces a phase shift, resulting in current oscillations relative to the chemical potential. Interestingly, adjusting  $\mu$  to 0.21 leads to a substantial overlap of chiral edge mode wavefunctions at both the left and right QAHI-SC interfaces due to their considerable broadening. This configuration triggers LARs at a single edge and within the inner QAHI region, giving rise to a  $\Phi_0$  periodicity in  $I_c$  (see Fig. 1(c)) [60].

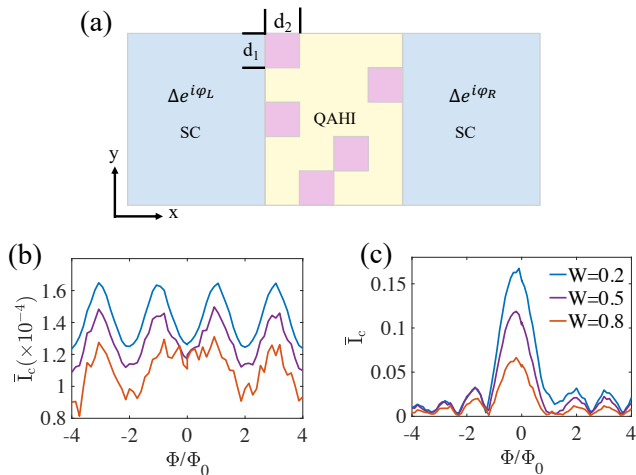


FIG. 5. (a) Schematic diagram of a QAH-based JJ with a random DW structure (top view). The DW size is denoted by  $d_1 \times d_2$ . The quantum interference patterns are affected by the different strengths of magnetic disorder  $W$  when (b)  $\mu = 0$  and (c)  $\mu = 1$ . In all cases, the DW size is  $d_1 \times d_2 = 10 \times 4$ , and the DW probability  $P = 0.5$ . We average over 50 random DW configurations.

To trace the evolution of the Josephson current from edge states to the bulk, we increase the chemical potential to  $\mu > 0.21$ , disrupting the previously observed  $2\Phi_0$  or  $\Phi_0$  periodicity. Interestingly, the Fraunhofer pattern with a distinct central peak of width  $2\Phi_0$  forms when  $\mu > 0.4$  (Figs. 3(d)-(f)), signaling the increased dominance of bulk states in the transport process. This occurrence correlates with the population of bulk carriers within the QAH region, leading to a consistent appearance of LARs at QAH-SC interfaces as  $\mu$  increases (refer to Fig. 1(d)). Due to the increase in bulk carriers, a noticeable enhancement in the maxima of  $I_c$  is also observed, as seen in Figs. 3(a)-(f), exceeding hundreds of times. Furthermore, the Fraunhofer pattern displays an asymmetric feature due to broken time-reversal symmetry, namely,  $I_c(M_z, \Phi) \neq I_c(M_z, -\Phi)$  when the magnetic field direction is reversed. Besides, the inversion symmetry invariance of  $I_c$  leads to the relationship  $I_c(M_z, \Phi) = I_c(-M_z, -\Phi)$  [61, 62]. In the subsequent calculations, we focus exclusively on the scenario where  $M_z = 0.3$  due to the aforementioned relationship. In summary,  $I_c$  of the QAH-based JJs can exhibit three distinct quantum interference patterns by tuning the chemical potential  $\mu$ : the unconventional  $2\Phi_0$ -periodic oscillation, the  $\Phi_0$ -periodic oscillation and the asymmetric Fraunhofer pattern.

To further reveal the origin of different interference patterns, we investigate the spatial distribution of local critical current  $j_c$  in the QAH region [57–59]. The local critical current is usually used to represent the current distribution of various systems, e.g., quantum Hall systems [63]. Figure 4 demonstrates the local current along the x-direction,  $j_c(y)$ , corresponding to the super-

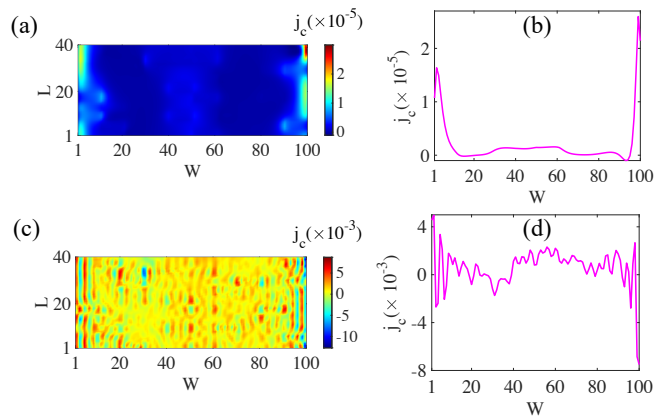


FIG. 6. The spatial distribution of local critical current in the QAH region [(a) and (c)] and at the QAH-SC interface [(b) and (d)] affected by the DW structure is examined under varying chemical potential values:  $\mu=0$  [(a),(b)] and 1 [(c),(d)]. In this case, the DW size is  $d_1 \times d_2 = 10 \times 4$ , the magnetic disorder strength  $W = 0.8$ , and the DW probability  $P = 0.5$ . In all cases,  $M_z = 0.3$ ,  $\Phi = 0$ , and the temperature  $T = \Delta/200$ .

conducting phase difference  $\varphi$ , precisely when the total current  $\sum_{y=1}^W j_c(y)$  reaches its maximum. At  $\mu = 0$ , the current predominantly flows along the QAH region's two edges, as evidenced in the spatial distribution of  $j_c$  displayed in Figs. 4(a) and (b). This observation aligns with the phenomenon depicted in Fig. 1(b), where transport within the central region is solely governed by the propagation of chiral edge carriers. Additionally, this current distribution is consistent with the quantum interference pattern shown in Fig. 3(a), characterized by a periodicity of  $2\Phi_0$ . Upon increasing  $\mu$  to 0.21, the edge current widens noticeably at the left and right QAH-SC interfaces as shown in Figs. 4(c) and (d). This visibly demonstrates the overlapping wavefunctions at these interfaces. Consequently, local Andreev pairs emerge both on a single edge and within the inner QAH region (see Fig. 1(c)), consistent with the scenario depicted in Fig. 3(c). Moreover, Figs. 4(e) and (f) show a bulk-dominated transport process, as the  $\mu$  value is further increased to 1. Thus, local Andreev pairs become uniformly distributed across the QAH region (see Fig. 1(d)), resulting in a Fraunhofer pattern, as observed in Fig. 3(f).

### C. Effects of domain walls

Given the inevitable appearance of DWs in magnetically doped topological insulators, we utilize a percolation model to simulate the effects of random DWs on quantum interference patterns [64]. Fig. 5(a) demonstrates the division of the central region into multiple blocks, each consisting of specific unit cells sized  $d_1 \times d_2$ .

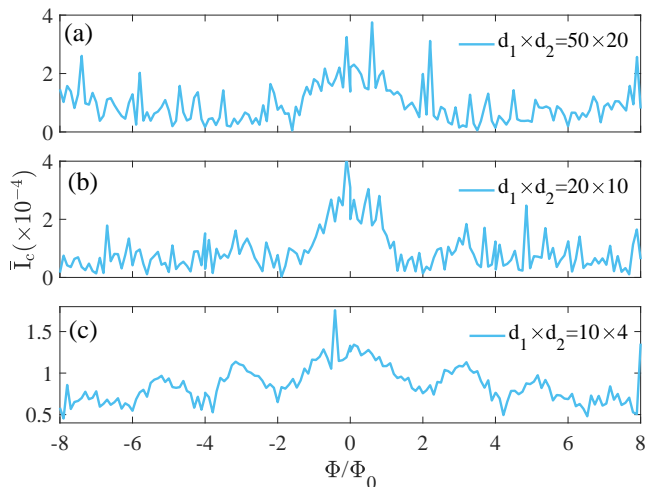


FIG. 7. The quantum interference patterns are affected by the DW structure at  $\mu = 0$  in a larger magnetic field range with different block sizes  $d_1 \times d_2$ : (a)  $50 \times 20$ , (b)  $20 \times 10$ , and (c)  $10 \times 4$ . In all cases, the magnetic disorder strength  $W = 1$  and the DW probability  $P = 0.5$ . We average over 15,25,50 random DW configurations in (a),(b), and (c), respectively.

The magnetization within each block is randomly chosen to potentially flip with a probability of  $P$ , while the flipped magnetization strength is uniformly distributed in the range of  $[-W/2, W/2]$  with the disorder strength  $W$ . The fragility of the  $\Phi_0$ -periodic oscillation pattern to the influence of DWs leads us to exclude its detailed discussion in this section.

In Figs. 5(b) and (c), we display the DW-averaged critical Josephson current, denoted as  $\bar{I}_c$ . Initially, focusing on the case with  $\mu = 0$  in Fig. 5(b), it is observed that  $\bar{I}_c$  remains relatively stable (in comparison with Fig. 3(a)) when  $W = 0.2$ , indicating the robustness of chiral edge states against weak magnetic disorder ( $W$ ). Then, at  $W = 0.5$ , the partial destruction of chiral edge modes diminishes the peak of the critical Josephson current  $\bar{I}_c$ . Despite DWs causing the emergence of some bulk carriers in the QAHI region, the  $2\Phi_0$  periodicity remains notably stable, owing to the dominance of transport by chiral edge modes. After that, increasing  $W$  to 0.8 initiates two simultaneous processes: the breakdown of chiral edge modes and a comparable contribution of bulk carriers to that of chiral edge carriers. Consequently, both the  $2\Phi_0$  periodicity and the characteristic shape of the quantum interference pattern are lost. Conversely, at  $\mu = 1$ , we observe remarkable stability in the interference pattern of bulk carriers, maintaining the shape of the asymmetric Fraunhofer pattern even at  $W = 0.8$ . This suggests that the unconventional  $2\Phi_0$ -periodic oscillation is more susceptible to disruption compared to the resilient nature of the asymmetric Fraunhofer pattern under DW structures. Furthermore, the values of  $\bar{I}_c$  gradually decrease with increasing  $W$  in Figs. 5(b) and (c), manifesting the influence of disorder effects.

Next, we examine the spatial distribution of the local

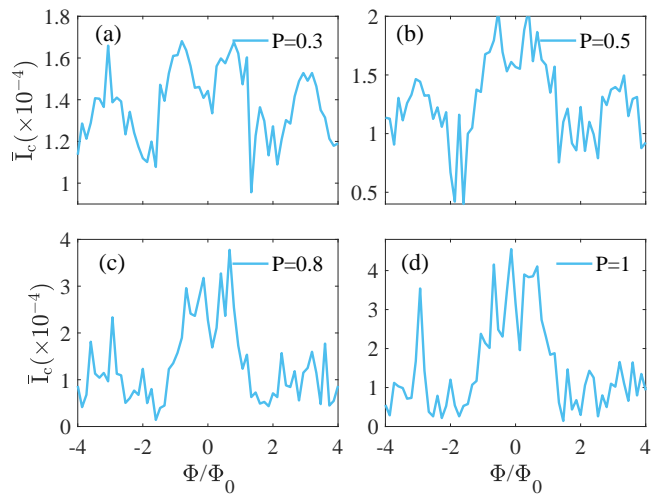


FIG. 8. The averaged critical Josephson currents  $\bar{I}_c$  vary with the DW probability  $P$  with  $\mu = 0$ ,  $W = 0.5$ , and  $d_1 \times d_2 = 20 \times 10$ . In all cases, we average over 25 random DW configurations.

critical current  $j_c$  within the QAHI region and at the QAHI-SC interface in Fig. 6, considering the existence of DW structures. In our calculation, we maintain a constant total magnetic flux  $\Phi = 0$  and compute the local current  $j_c(y)$  along the x-direction when the total current  $\sum_{y=1}^W j_c(y)$  reaches its maximum. Due to the presence of DW structures, the local critical current  $j_c$  exhibits static eddy-like currents in addition to constant currents. In Figs. 6(a) and (b) at  $\mu = 0$ , it is evident that the chiral edge modes are disrupted, and some bulk carriers emerge within the inner QAHI region due to the random distribution of DWs across the QAHI region. This observation aligns with the behavior depicted in the curve corresponding to  $W = 0.8$  in Fig. 5(b). Conversely, when  $\mu = 1$ , the distribution of  $j_c$  exhibits characteristics akin to typical bulk transport, facilitating the stability of the asymmetric Fraunhofer pattern within DW structures. Notably, in Figs. 6(c) and (d),  $j_c$  values oscillate more prominently compared to Figs. 4(c) and (d).

To gain deeper insights into how DWs affect the edge current, we explore the quantum interference pattern at  $\mu = 0$  by varying the sizes of DWs under a strong magnetic disorder strength  $W = 1$ , spanning a wider range of magnetic fields. In Fig. 7(a), an emergent central lobe is observed within the interval  $\Phi/\Phi_0 \in (-2, 2)$ , alongside side lobes at higher values of  $\Phi$ . Notably, the average critical current  $\bar{I}_c$  displays significant fluctuations, which can be attributed to the presence of DWs. Additionally, the increase in the maxima of the central lobe is linked to the emergence of bulk carriers caused by a limited number of DWs, particularly when the DW size is  $d_1 \times d_2 = 50 \times 20$ . This interference pattern remarkably resembles to the Fraunhofer pattern illustrated in Fig. 3(f). The emergence of bulk carriers in the QAHI

region due to the presence of DWs is the underlying cause of this phenomenon. When we decrease the DW size to  $d_1 \times d_2 = 20 \times 10$  to allow for a larger quantity of DWs, a more distinct Fraunhofer-like pattern is evident within the  $\bar{I}_c$  values in Fig. 7(b). Again, the presence of bulk carriers contributes to the enhancement of maxima of the central lobe, compared to the scenario depicted in Fig. 3(a). When the DW size is further decreased to  $d_1 \times d_2 = 10 \times 4$ , as depicted in Fig. 7(c), the increased visibility of the periodicity in the higher lobes reveals a distinct Fraunhofer-like pattern. In particular, the periods of the central and side lobes are twice those of the conventional Fraunhofer pattern. To conclude, the observed Fraunhofer-like pattern in chiral JJs likely extends beyond our model and is prevalent in those doped with magnetic impurities, holding promise for further experimental verification.

At last, we briefly discuss another factor affecting the behavior of the quantum interference pattern in DW structures: the DW probability  $P$ , as illustrated in Fig. 8. With an increase in  $P$ , more DWs emerge in the QAHI region, leading to an evolution of the interference pattern toward a Fraunhofer-like pattern, aligning with our previous analysis. In summary, the interference pattern within the DW structure can be influenced by factors such as magnetic disorder strength  $W$ , DW size  $d_1 \times d_2$ , and DW probability  $P$ .

#### IV. CONCLUSION

In this work, we explore the transport properties of the chiral JJs based on the QAHI connecting to two s-

wave superconducting electrodes, through numerical calculation of the Josephson current ( $I_c$ ). We present a systematic crossover from edge-state to bulk-state dominated supercurrents, with a notable  $0 - \pi$  transition that becomes apparent with adjustments in the chemical potentials under non-zero magnetic flux. This transition shows the competition between bulk and chiral edge transport. Moreover, we find an evolution among three distinct quantum interference patterns through adjustments in the chemical potentials: from a  $2\Phi_0$ -periodic oscillation pattern, to a  $\Phi_0$ -periodic oscillation pattern, and then to an asymmetric Fraunhofer pattern. Finally, a Fraunhofer-like pattern, with periods twice those of the conventional one, emerges due to the coexistence of the chiral edge state and the domain wall states, even when the chemical potential resides within the gap. This phenomenon is likely widespread in chiral JJs doped with magnetic impurities. Our findings also hold promise for direct experimental verification.

#### ACKNOWLEDGMENTS

The authors would like to thank Yang Feng, Yu-Hang Li, and Qing Yan for helpful discussions. We are grateful to the support by the National Key R&D Program of China (Grants No. 2022YFA1403700), the National Natural Science Foundation of China (Grant No.12204053), and the Innovation Program for Quantum Science and Technology (Grant No.2021ZD0302400). C.-Z. Chen is also support by the Natural Science Foundation of Jiangsu Province Grant (No. BK20230066) and the Priority Academic Program Development (PAPD) of Jiangsu Higher Education Institution.

- 
- [1] F. D. M. Haldane, *Phys. Rev. Lett.* **61**, 2015 (1988).
  - [2] C.-X. Liu, S.-C. Zhang, and X.-L. Qi, *Annu. Rev. Condens. Matter Phys.* **7**, 301(2016).
  - [3] C.-Z. Chang, C.-X. Liu, and A. H. MacDonald, *Rev. Mod. Phys.* **95**, 011002 (2023).
  - [4] R. Chen, H.-P. Sun, B. Zhou, and D.-H. Xu, *Sci. China: Phys. Mech. Astron.* **66**, 287211 (2023).
  - [5] C.-X. Liu, X.-L. Qi, X. Dai, Z. Fang, and S.-C. Zhang, *Phys. Rev. Lett.* **101**, 146802 (2008).
  - [6] X.-L. Qi, T. L. Hughes, and S.-C. Zhang, *Phys. Rev. B* **78**, 195424 (2008).
  - [7] R. Yu, W. Zhang, H. J. Zhang, S. C. Zhang, X. Dai, and Z. Fang, *Science* **329**, 61 (2010).
  - [8] C.-Z. Chang, J. Zhang, X. Feng, J. Shen, Z. Zhang, M. Guo, K. Li, Y. Ou, P. Wei, L.-L. Wang, Z.-Q. Ji, Y. Feng, S. Ji, X. Chen, J. Jia, X. Dai, Z. Fang, S.-C. Zhang, K. He, Y. Wang, L. Lu, X.-C. Ma, and Q.-K. Xue, *Science* **340**, 167 (2013).
  - [9] M. Mogi, R. Yoshimi, A. Tsukazaki, K. Yasuda, Y. Kozuka, K. S. Takahashi, M. Kawasaki, and Y. Tokura, *Appl. Phys. Lett.* **107**, 182401 (2015).
  - [10] Y. Ou, C. Liu, G. Jiang, Y. Feng, D. Zhao, W. Wu, X.-X. Wang, W. Li, C. Song, L.-L. Wang, W. Wang, W. Wu, Y. Wang, K. He, X.-C. Ma, and Q.-K. Xue, *Adv. Mater.* **30**, 1703062 (2018).
  - [11] J. G. Checkelsky, R. Yoshimi, A. Tsukazaki, K. S. Takahashi, Y. Kozuka, J. Falson, M. Kawasaki, and Y. Tokura, *Nat. Phys.* **10**, 731 (2014).
  - [12] X. Kou, S.-T. Guo, Y. Fan, L. Pan, M. Lang, Y. Jiang, Q. Shao, T. Nie, K. Murata, J. Tang, Y. Wang, L. He, T.-K. Lee, W.-L. Lee, and K. L. Wang, *Phys. Rev. Lett.* **113**, 137201 (2014).
  - [13] A. J. Bestwick, E. J. Fox, X. Kou, L. Pan, K. L. Wang, and D. Goldhaber-Gordon, *Phys. Rev. Lett.* **114**, 187201 (2015).
  - [14] A. Kandala, A. Richardella, S. Kempinger, C.-X. Liu, and N. Samarth, *Nat. Commun.* **6**, 7434 (2015).
  - [15] Ella O. Lachman, A. F. Young, A. Richardella, J. Cuppens, H. R. Naren, Y. Anahory, A. Y. Meltzer, A. Kandala, S. Kempinger, Y. Myasoedov, M. E. Huber, N. Samarth, and E. Zeldov, *Sci. Adv.* **1**, e1500740 (2015).
  - [16] M. Liu, W. Wang, A. R. Richardella, A. Kandala, J. Li, A. Yazdani, N. Samarth, and N. P. Ong, *Sci. Adv.* **2**,

- e1600167 (2016).
- [17] M. Kawamura, R. Yoshimi, A. Tsukazaki, K. S. Takahashi, M. Kawasaki, and Y. Tokura, *Phys. Rev. Lett.* **119**, 016803 (2017).
- [18] C.-Z. Chang, W. Zhao, D. Y. Kim, H. Zhang, B. A. Assaf, D. Heiman, S.-C. Zhang, C. Liu, M. H. Chan, and J. S. Moodera, *Nat. Mater.* **14**, 473 (2015).
- [19] C.-Z. Chang, W. Zhao, D. Y. Kim, P. Wei, J. K. Jain, C. Liu, M. H. W. Chan, and J. S. Moodera, *Phys. Rev. Lett.* **115**, 057206 (2015).
- [20] S. Grauer, S. Schreyeck, M. Winnerlein, K. Brunner, C. Gould, and L. W. Molenkamp, *Phys. Rev. B* **92**, 201304(R) (2015).
- [21] S. Grauer, K. M. Fijalkowski, S. Schreyeck, M. Winnerlein, K. Brunner, R. Thomale, C. Gould, and L. W. Molenkamp, *Phys. Rev. Lett.* **118**, 246801 (2017).
- [22] G. Lippertz, A. Bliesener, A. Uday, L. M. C. Pereira, A. A. Taskin, and Y. Ando, *Phys. Rev. B* **106**, 045419 (2022).
- [23] Y. Deng, Y. Yu, M. Z. Shi, Z. Guo, Z. Xu, J. Wang, X. H. Chen, and Y. Zhang, *Science* **367**, 895 (2020).
- [24] Y. Gong, J. Guo, J. Li, K. Zhu, M. Liao, X. Liu, Q. Zhang, L. Gu, L. Tang, and X. Feng, *Chin. Phys. Lett.* **36**, 076801 (2019).
- [25] M. M. Otrokov, I. I. Klimovskikh, H. Bentmann, D. Estyunin, A. Zeugner, Z. S. Aliev, S. Gaß, A. U. B. Wolter, A. V. Koroleva, A. M. Shikin, M. Blanco-Rey, M. Hoffmann, I. P. Rusinov, A. Yu. Vyazovskaya, S. V. Ereameev, Yu. M. Koroteev, V. M. Kuznetsov, F. Freyse, J. Sánchez-Barriga, I. R. Amiraslanov, M. B. Babanly, N. T. Mamedov, N. A. Abdullayev, V. N. Zverev, A. Alfonso, V. Kataev, B. Büchner, E. F. Schwier, S. Kumar, A. Kimura, L. Petaccia, G. Di Santo, R. C. Vidal, S. Schatz, K. Kißner, M. Ünzelmann, C. H. Min, Simon Moser, T. R. F. Peixoto, F. Reinert, A. Ernst, P. M. Echenique, A. Isaeva, and E. V. Chulkov, *Nature (London)* **576**, 416 (2019).
- [26] A. L. Sharpe, E. J. Fox, A. W. Barnard, J. Finney, K. Watanabe, T. Taniguchi, M. Kastner, and D. Goldhaber-Gordon, *Science* **365**, 605 (2010).
- [27] M. Serlin, C. Tschirhart, H. Polshyn, Y. Zhang, J. Zhu, K. Watanabe, T. Taniguchi, L. Balents, and A. Young, *Science* **367**, 900 (2020).
- [28] T. Li, S. Jiang, B. Shen, Y. Zhang, L. Li, Z. Tao, T. Devakul, K. Watanabe, T. Taniguchi, L. Fu, J. Shan, and K. F. Mak, *Nature* **600**, 641 (2021).
- [29] X.-L. Qi and S.-C. Zhang, *Rev. Mod. Phys.* **83**, 1057 (2011).
- [30] J. Wang, Q. Zhou, B. Lian, and S.-C. Zhang, *Phys. Rev. B* **92**, 064520 (2015).
- [31] A. Uday, G. Lippertz, K. Moors, H. F. Legg, A. Bliesener, L. M. C. Pereira, A. A. Taskin, and Y. Ando, *arXiv:2307.08578*.
- [32] M. Kayyalha1, D. Xiao, R. Zhang, J. Shin, J. Jiang, F. Wang, Y.-F. Zhao, R. Xiao, L. Zhang, K. M. Fijalkowski, P. Mandal, M. Winnerlein, C. Gould, Q. Li, L. W. Molenkamp, M. H. W. Chan, N. Samarth, and C.-Z. Chang, *Science* **367**, 6473 (2020).
- [33] H. Yi, Y.-F. Zhao, Y.-T. Chan, J. Cai, R. Mei, X. Wu, Z.-J. Yan, L.-J. Zhou, R. Zhang, Z. Wang, S. Paolini, R. Xiao, K. Wang, A. R. Richardella, J. Singleton, L. E. Winter, T. Prokscha, Z. Salman, A. Suter, P. P. Balakrishnan, A. J. Grutter, M. H. W. Chan, N. Samarth, X. Xu, W. Wu, C.-X. Liu, C.-Z. Chang, *arXiv:2312.04353*.
- [34] L. Fu and C. L. Kane, *Phys. Rev. Lett.* **100**, 096407 (2008).
- [35] X.-L. Qi, T. L. Hughes, and S.-C. Zhang, *Phys. Rev. B* **82**, 184516 (2010).
- [36] J. Alicea, *Rep. Prog. Phys.* **75**, 076501 (2012).
- [37] C. Beenakker, *Annu. Rev. Condens. Matter Phys.* **4**, 113 (2013).
- [38] M. Sato and Y. Ando, *Rep. Prog. Phys.* **80**, 076501 (2017).
- [39] A. Yazdani, F. von Oppen, B. I. Halperin, and A. Yacoby, *Science* **380**, eade0850 (2023).
- [40] N.-X. Yang, Q. Yan, and Q.-F. Sun, *Phys. Rev. B* **105**, 125414 (2022).
- [41] A. Ii, K. Yada, M. Sato, and Y. Tanaka, *Phys. Rev. B* **83**, 224524 (2011).
- [42] Y.-F. Zhou, Z. Hou, P. Lv, X. C. Xie, and Q.-F. Sun, *Sci. China: Phys. Mech. Astron.* **61**, 127811 (2018).
- [43] K. Sakurai, S. Ikegaya, and Y. Asano, *Phys. Rev. B* **96**, 224514 (2017).
- [44] C.-Z. Chen, J. J. He, D.-H. Xu, and K. T. Law, *Phys. Rev. B* **98**, 165439 (2018).
- [45] Q. Yan, Y.-F. Zhou, and Q.-F. Sun, *Chin. Phys. B* **29**, 097401 (2020).
- [46] Ryota Nakai, Kentaro Nomura, and Yukio Tanaka, *Phys. Rev. B* **103**, 184509 (2021).
- [47] Q. Cheng, Q. Yan, and Q.-F. Sun, *Phys. Rev. B* **104**, 134514 (2021).
- [48] A. F. Andreev, *Sov. Phys. JETP* **19**, 1228–1234 (1964).
- [49] M. Ma and A. Yu. Zyuzin, *Europhys. Lett.* **21**, 941 (1993).
- [50] A. Yu. Zyuzin, *Phys. Rev. B* **50**, 323 (1994).
- [51] D. S. Shapiro, A. Shnirman, and A. D. Mirlin, *Phys. Rev. B* **93**, 155411 (2016).
- [52] J. Liu, H. Liu, J. Song, Q.-F. Sun, and X. C. Xie, *Phys. Rev. B* **96**, 045401 (2017).
- [53] J. A. M. Van Ostaay, A. R. Akhmerov, and C. W. J. Beenakker, *Phys. Rev. B* **83**, 195441 (2011).
- [54] Y. Alavirad, J. Lee, Z.-X. Lin, and J. D. Sau, *Phys. Rev. B* **98**, 214504 (2018).
- [55] R. Yu, W. Zhang, H. J. Zhang, S. C. Zhang, X. Dai, and Z. Fang, *Science* **329**, 61 (2010).
- [56] J. Wang, B. Lian, and S. C. Zhang, *Phys. Rev. B* **89**, 085106 (2014).
- [57] A. Furusaki, *Phys. B: Condens. Matter* **203**, 214 (1994).
- [58] Y. Asano, *Phys. Rev. B* **63**, 052512 (2001).
- [59] Y. Asano, Y. Tanaka, M. Sigrist, and S. Kashiwaya, *Phys. Rev. B* **67**, 184505 (2003).
- [60] Z.-T. Sun, J.-X. Hu, Y.-M. Xie, and K. T. Law, *arxiv:2308.01079*.
- [61] K. Saitoh, S. Kashiwaya, H. Kashiwaya, Y. Mawatari, Y. Asano, Y. Tanaka, and Y. Maeno, *Phys. Rev. B* **92**, 100504(R) (2015).
- [62] S. Kashiwaya, K. Saitoh, H. Kashiwaya, M. Koyanagi, M. Sato, K. Yada, Y. Tanaka, and Y. Maeno, *Phys. Rev. B* **100**, 094530 (2019).
- [63] H. Li, H. Jiang, Q.-F. Sun, and X. C. Xie, *arxiv:2303.07692* (2023).
- [64] Y.-H. Li, J. Liu, H. Liu, H. Jiang, Q.-F. Sun, and X. C. Xie, *Phys. Rev. B* **98**, 045141 (2018).